Dyson norms in XUV and strong-field ionization of polyatomics: Cytosine and uracil

Michael Spanner,[1] Serguei Patchkovskii,[1] Congyi Zhou,[2] Spiridoula Matsika,[2] Marija Kotur,[3] and Thomas C. Weinacht[3]
[1]*Steacie Institute for Molecular Sciences, National Research Council of Canada, Ottawa, Ontario, Canada K1A 0R6*
[2]*Department of Chemistry, Temple University, Philadelphia, Pennsylvania 19122, USA*
[3]*Department of Physics, Stony Brook University, Stony Brook, New York 11794, USA*
(Received 24 May 2012; published 5 November 2012)

The extreme-ultraviolet (XUV) and strong-field valence ionization of cytosine and uracil is considered. We examine some simple estimates of the relative yields of the cation states populated following ionization and compare these to the results of a recently developed *ab initio*–type numerical model designed to compute strong-field ionization of molecules, the so-called time-dependent resolution in ionic states (TD-RIS) method. In analogy with one-photon XUV ionization, where the photoionization matrix elements can be related to the Dyson orbitals, we construct estimates for the yield of strong-field ionization (SFI) to different cation states based on the Dyson orbital norms and the Keldysh tunneling ionization rate. In the case of XUV ionization, the Dyson norms are shown to be good predictors of the relative cation yields when compared with the TD-RIS yields. The Dyson- and Keldysh-based models underestimate the yield to excited cation states in the case of SFI. The increased yield to the excited cation states in the TD-RIS results is attributed to the inclusion of multielectron effects and continuum structure not present in the simple models. The molecular Ammosov-Delone-Krainov (MO-ADK) method of calculating SFI is also considered. This later method is seen to agree more closely with the Dyson- and Keldysh-based estimates as it also fails to capture the multielectron effects and continuum structure included in the TD-RIS approach.

DOI: 10.1103/PhysRevA.86.053406 PACS number(s): 33.80.Rv, 33.80.Eh

I. INTRODUCTION

The emergence of attosecond science [1], driven largely by advances in strong-field and recollision physics [2] that lead to high-order-harmonic generation (HHG) and the realization of attosecond XUV pulses, has stimulated an interest in accurate descriptions of molecular strong-field ionization (SFI) and attosecond XUV ionization. Pump-probe spectroscopies using attosecond XUV pulses would likely involve attosecond XUV ionization as the probing step [3], and attosecond probing techniques [4] that rely directly on the process of HHG necessarily involve strong-field ionization as the first step in HHG. In addition to these attosecond techniques, strong-field ionization itself is being explored as a probe of electronic [5] and nuclear [6] dynamics in molecules.

In this study, we consider both attosecond XUV ionization and SFI of ground and excited states of cytosine and uracil. The valence excited states of these molecules have been studied extensively in the past, as they play an important role in the interaction of DNA and RNA with UV radiation. Some of the techniques used for elucidating the excited-state dynamics include pump-probe techniques, with SFI as a probe. Even though this is not the focus of this paper, the findings of our work may prove helpful in interpreting these experiments. Both cytosine and uracil are heterocyclic organic molecules and have multiple excited states in the UV energy range. The first excited state (S_1) in cytosine is a bright $\pi\pi^*$ state, whereas in uracil S_1 is a dark $n\pi^*$ state and the second excited state (S_2) is a bright $\pi\pi^*$. So, in our calculations we include ionization from S_1 for cytosine and from S_1 and S_2 for uracil. The orbitals involved in the excitation and the electronic configurations are shown in Appendix D.

The process of gas-phase molecular photoionization by ultrafast pulses of radiation would, of course, be most accurately described by a full-dimensionality solution of the time-dependent Schrödinger equation. However, such a full-dimensionality solution is typically impossible due to the exponential increase of the computation complexity with increasing dimensionality. Furthermore, even if such a solution was routinely available, the desire for physically intuitive approximations that offer satisfying conceptual frameworks for thinking about the problem would remain. Since the earliest days of quantum mechanics, a particularly useful picture of one-photon XUV and x-ray photoionization follows from Koopmans' theorem [7]. Designed to predict ionization energies, Koopmans' theorem (i) assumes a Hartree-Fock molecular-orbital description of the multielectronic states of the neutral and cation species and (ii) ignores orbital relaxation in the cation following photoionization. The photoionization process is then seen as the removal of an electron from specific single-particle orbitals of the neutral. Predicting the relative probabilities of photoionization to different cation states often requires going one step beyond the Koopmans' picture. Standard approximations developed for XUV and x-ray photoionization that do not rely on the assumption inherent in Koopmans' theorem, like the sudden approximation and/or one-photon perturbation theory, lead to the concept of Dyson orbitals [8,9]. Dyson orbitals represent overlaps between the neutral and cation multielectron wave functions and are routinely used in theoretical studies of XUV ionization in the perturbative regime [10]. The norms of the Dyson orbitals then become good predictors of the relative yields of the possible ionizing transitions.

In this paper, we explore the strong-field ionization of the polyatomic molecules cytosine and uracil and attempt to answer the question whether Dyson orbitals and Dyson norms alone can qualitatively capture the behavior of SFI. In parallel, we consider the XUV ionization of the same species in order to provide a guiding example of the utility of Dyson

orbitals for one-photon ionization. Since our main interest is in SFI, we consider ionization from the outer valence shell only—the dominant channel for SFI. We first outline the key analytical approximations that relate one-photon ionization and SFI to the Dyson orbitals: the sudden approximation and one-photon perturbation theory for XUV ionization, and the strong-field approximation (SFA) for SFI. We then present the results of our numerical calculations for the XUV ionization and SFI of these molecules using the recently developed time-dependent ionization formalism of Ref. [11], herein called the time-dependent resolution in ionic states (TD-RIS) method. We compare the results of the TD-RIS computations with predictions based on the simple analytical treatments related to the Dyson norms, as well as to predictions from the molecular Ammosov-Delone-Krainov (MO-ADK) theory [12,13], a popular quasistatic theory of molecular ionization based on semiclassical tunneling models. As expected, the Dyson norms are seen to be adequate predictors of total ionization yields in the case of one-photon XUV ionization. Analogous simple analytical treatments involving the Dyson norms do not ultimately offer a quantitatively accurate picture of SFI. Although Dyson norms alone do not fully capture the behavior of SFI, the analysis of where, and why, these ideas break down provides a clear framework for discussing and understanding non-Dyson effects in molecular SFI.

II. ANALYTICAL CONSIDERATIONS AND MOTIVATION

A. Dyson orbitals

Given the neutral state $|N_m\rangle$ and ionic states $|I_l\rangle$, a set of single-particle orbitals arises naturally for the present problem, called Dyson orbitals [8,9], defined as the overlap between the neutral and ionic states:

$$\left|\phi^{\mathrm{D}}_{lm}\right\rangle = \sqrt{n}\langle I_l|N_m\rangle. \tag{1}$$

The integral implied by the brackets in Eq. (1) is taken over the $(n-1)$ ionic electrons, and the Dyson orbitals are thus one-electron functions. Unlike atomic or molecular orbitals typically used in electronic structure theories, the Dyson orbitals do not in general have unit norms. It is then convenient to write the Dyson orbitals as

$$\left|\phi^{\mathrm{D}}_{lm}\right\rangle = \eta_{lm}\left|\tilde{\phi}^{\mathrm{D}}_{lm}\right\rangle, \tag{2}$$

where

$$\left|\tilde{\phi}^{\mathrm{D}}_{lm}\right\rangle = \frac{\left|\phi^{\mathrm{D}}_{lm}\right\rangle}{\sqrt{\left\langle\phi^{\mathrm{D}}_{lm}\middle|\phi^{\mathrm{D}}_{lm}\right\rangle}} \tag{3}$$

are normalized Dyson orbitals, and the amplitudes η_{lm} are given by

$$\eta_{lm} = \left\langle\tilde{\phi}^{\mathrm{D}}_{lm}\middle|\phi^{\mathrm{D}}_{lm}\right\rangle. \tag{4}$$

The Dyson norms are defined as

$$G^{\mathrm{D}}_{lm} = |\eta_{lm}|^2 = \left\langle\phi^{\mathrm{D}}_{lm}\middle|\phi^{\mathrm{D}}_{lm}\right\rangle. \tag{5}$$

B. Continuum functions

A number of different assumptions can be made for the continuum states. We work with multielectron continuum-ion wave functions that, in principle, have the form

$$|M_m\rangle = \widehat{\mathcal{A}}\,|I_m(x_1,\ldots,x_{n-1})\rangle\left|\phi^{\vec{k}}_m(x_n)\right\rangle, \tag{6}$$

where $|\phi^{\vec{k}}_m(x_n)\rangle$ is a continuum state with momentum $\vec{k}$, and $\widehat{\mathcal{A}}$ is the appropriate antisymmetrizer [14]. At this stage, the continuum function $|\phi^{\vec{k}}_m(x_n)\rangle$ could be either a plane wave or a distorted wave that takes effects of the ionic core on the continuum into account. In the following, which function is being used for $|\phi^{\vec{k}}_m(x_n)\rangle$ is specified when the particular form of the continuum matters. Although the states $|M_m\rangle$ each include only a single cation configuration, they can be used to construct multiconfigurational continuum-ion states

$$|\mathcal{M}_j\rangle = \sum_m |M_m\rangle = \sum_m \widehat{\mathcal{A}}\,|I_m\rangle\left|\phi^{\vec{k}}_m\right\rangle. \tag{7}$$

Note that in Eq. (7) the $|\phi^{\vec{k}}_m\rangle$ need not be normalized to 1. Rather, the weight of each ionic channel is carried by the normalization of the populated continuum functions $|\phi^{\vec{k}}_m\rangle$.

C. XUV ionization

1. *Sudden approximation*

As a starting point for the discussion, consider two simple treatments of relative yields of one-photon XUV ionization [8]. The first treatment is offered by the sudden approximation as applied to the Hamiltonian [8], which proceeds as follows. Before the ionization event, all electrons interact and the relevant multielectron Hamiltonian contains all electron-electron interaction terms. After the ionization, one electron is free and no longer interacts with the remaining bound electrons. The multielectron states then have the form of the $|M_m\rangle$ states. Projecting the initial state of the system onto the final state then gives an estimate of the transition probability for ionization:

$$w^{\mathrm{sud}}_{lm}(\vec{k}) = |\langle M_l|N_m\rangle|^2 = \left|\left(\left\langle\phi^{\vec{k}}_l\right|\langle I_l|\widehat{\mathcal{A}}\right)|N_m\rangle\right|^2 = \left|\left\langle\phi^{\vec{k}}_m\middle|\phi^{\mathrm{D}}_{lm}\right\rangle\right|^2. \tag{8}$$

In the notation of the normalized Dyson orbitals, w^{sud}_{lm} becomes

$$w^{\mathrm{sud}}_{lm}(\vec{k}) = \left|\left\langle\phi^{\vec{k}}_m\middle|\tilde{\phi}^{\mathrm{D}}_{lm}\right\rangle\right|^2 G^{\mathrm{D}}_{lm}, \tag{9}$$

and integrating over all $\vec{k}$ gives the total yield

$$W^{\mathrm{sud}}_{lm} = \int d\vec{k}\; w^{\mathrm{sud}}_{lm}(\vec{k}) = \left(\int d\vec{k}\;\left|\left\langle\phi^{\vec{k}}_m\middle|\tilde{\phi}^{\mathrm{D}}_{lm}\right\rangle\right|^2\right) G^{\mathrm{D}}_{lm}. \tag{10}$$

Equations (9) and (10) show that, when little continuum structure is expected (i.e., $\int d\vec{k}\;|\langle\phi^{\vec{k}}_m|\tilde{\phi}^{\mathrm{D}}_{lm}\rangle|^2 \approx \text{const}$), W^{sud}_{lm} is expected to be proportional to the norm of the Dyson orbitals, G^{D}_{lm}.

2. *One-photon perturbation theory*

A second (and more accurate) treatment of XUV ionization uses first-order time-dependent perturbation theory to calculate the one-photon ionization probability. The first-order

ionization probability is given by

$$w_{lm}^{1st}(\vec{k}) = |\mathcal{F}(\omega_k)|^2 |\langle M_l| \sum_j \vec{\epsilon}_F \cdot \vec{r}_j |N_m\rangle|^2$$
$$= |\mathcal{F}(\omega_k)|^2 \left|\langle \phi_l^{\vec{k}} | \vec{\epsilon}_F \cdot \vec{r}_n | \phi_{lm}^{D}\rangle + \langle \phi_l^{\vec{k}} | \phi_{lm}^{C}\rangle\right|^2, \quad (11)$$

where $\mathcal{F}(\omega)$ is the frequency spectrum of the laser pulse,

$$\mathcal{F}(\omega) = \frac{1}{\sqrt{2\pi}} \int dt\, e^{i\omega t} F(t), \quad (12)$$

$\omega_k = |\vec{k}|^2/2 + E^I - E_m^N$ is the energy of the photon absorbed in order to eject an electron with momentum $\vec{k}$, and the orbitals $|\phi_{lm}^C\rangle$ are given by

$$|\phi_{lm}^C\rangle = \langle I_m| \sum_{j=1}^{n-1} \vec{\epsilon}_F \cdot \vec{r}_j |N_m\rangle. \quad (13)$$

Within the assumption of strong orthogonality, where the continuum functions $|\phi_l^{\vec{k}}\rangle$ are assumed to be orthogonal to all the bound orbitals contained in $|N_m\rangle$ and $|I_m\rangle$, the $\langle \phi_l^{\vec{k}} | \phi_{lm}^C\rangle$ term would be zero, and $w_{lm}^{1st}(\vec{k})$ becomes [8]

$$w_{lm}^{1st}(\vec{k}) = |\mathcal{F}(\omega_k)|^2 \left|\langle \phi_l^{\vec{k}} | \vec{\epsilon}_F \cdot \vec{r}_n | \tilde{\phi}_{lm}^{D}\rangle\right|^2 G_{lm}^{D}, \quad (14)$$

and the total yield becomes

$$W_{lm}^{1st} = \left(\int d\vec{k}\, |\mathcal{F}(\omega_k)|^2 \left|\langle \phi_l^{\vec{k}} | \vec{\epsilon}_F \cdot \vec{r}_n | \tilde{\phi}_{lm}^{D}\rangle\right|^2 \right) G_{lm}^{D}. \quad (15)$$

These terms are kept in the time-dependent numerical simulations presented below. Equations (14) and (15) show that the Dyson norms G_{lm}^D again appear in the first-order expression for the transition probability, and one could still expect that the G_{lm}^D could act as rough predictors of the relative ionization probability to the available ionic states, with the assumption that the matrix elements $|\langle \phi_l^{\vec{k}} | \vec{\epsilon}_F \cdot \vec{r}_n | \tilde{\phi}_{lm}^D\rangle|^2$ are slowly varying and carry little structure.

D. Strong-field ionization

Consider now low-frequency SFI. The standard model of SFI is the SFA, which calculates the ionization amplitudes within an S-matrix formalism. The continuum states are taken as free-electron solutions in the laser field alone, ignoring the effects of the ionic electrostatic potential on these states. This treatment of the continuum is qualitatively similar to the first Born approximation of scattering states with the addition that the action of the laser is taken fully into account. Allowing the laser field to act on one electron only (the single-active electron approximation, almost universally invoked in SFA treatments of strong-field effects), the SFA probability for ionization of a multielectron target, leading to a continuum electron with momentum $\vec{k}$, can be written as

$$w_{lm}^{SFA}(\vec{k}) = \left|\langle \phi_l^{\vec{k}} | U^{SFA} | \tilde{\phi}_{lm}^{D}\rangle\right|^2 G_{lm}^{D}, \quad (16)$$

where the SFA propagator is given by

$$U^{SFA} = -i \int dt' \int d\vec{k}\, |\phi_l^{\vec{k}}\rangle \exp\left[-\frac{i}{2}\int_{t'}^{t} |\vec{k} + \vec{A}(\tau)|^2 d\tau\right]$$
$$\times e^{i I_{p,lm} t'} \langle \phi_l^{\vec{k}} | V(t') \quad (17)$$

where

$$V(t) = \sum_{j=1}^{n} F(t)\, \vec{\epsilon}_F \cdot \vec{r}_j, \quad (18)$$

$F(t)$ is the time-dependent electric field of the laser, $\vec{\epsilon}_F$ is the polarization direction, and $I_{p,lm} = E_I^l - E_N^m$ is the ionization potential. The integral in Eq. (17) can be solved using approaches based on stationary phase and/or semiclassical approximations [15–17]. Following integration, the total yield can be written as

$$W_{lm}^{SFA} = C_{lm}\, K(I_{p,lm}, F_0)\, G_{lm}^{D}, \quad (19)$$

where

$$K(I_{p,lm}, F_0) = \exp\left[-\frac{2}{3}\frac{(2I_{p,lm})^{3/2}}{|F_0|}\right] \quad (20)$$

is the dominant exponential factor of the Keldysh tunnel ionization rate [15]. The prefactor C_{lm} depends weakly (i.e., not exponentially) on F_0 and $I_{p,lm}$ as well as on the specific state (or Dyson orbital) being ionized.

In analogy with the above arguments for one-photon XUV ionization, which showed that the Dyson norms G_{lm}^D could be used as rough approximations to the relative ionization probabilities, Eq. (19) suggests that a good predictor of SFI probabilities might be given by

$$W_{lm}^{DK} = K(I_{p,lm}, F_0)\, G_{lm}^{D}, \quad (21)$$

where only the exponential Keldysh rate is retained. This approximation, which we call the Dyson-Keldysh (DK) estimate, assumes that the C_{lm} factors do not greatly affect the relative ionization probabilities, in analogy with the assumption that the $|\langle \phi_l^{\vec{k}} | \tilde{\phi}_{lm}^D\rangle|^2$ and $|\langle \phi_l^{\vec{k}} | \vec{\epsilon}_F \cdot \vec{r}_n | \tilde{\phi}_{lm}^D\rangle|^2$ can be neglected for one-photon XUV ionization.

E. TD-RIS

The construction and final equations of the TD-RIS formalism are outlined in the Appendixes. The two central approximations are that the continuum electron is not antisymmetrized with the remaining bound electrons upon ionization, and only a finite number of cationic states are included. The method includes a number of effects typically neglected in semianalytical approaches to strong-field ionization like Keldysh- or SFA-based methods, including the MO-ADK approach considered below. For example, TD-RIS includes the effects of the ionic binding potential on the continuum wave packet during ionization and also includes correctly the influence of orbital symmetries and structure of the initial Dyson orbital. Furthermore, TD-RIS includes multichannel coupling where ionic transitions are possible during the ionization event due to Coulomb interaction between the outgoing electron and the ionic core—the outgoing electron can cause transition in the ionic core due to Coulomb interactions. The Coulomb interactions are found to be important in the context of low-frequency strong-field ionization and are discussed further in Sec. III B. In principle, effects of laser-driven dipole coupling between the neutral and ionic states could also be included. These latter couplings are neglected in the present study. However, we do briefly consider their potential influence in the Appendixes.

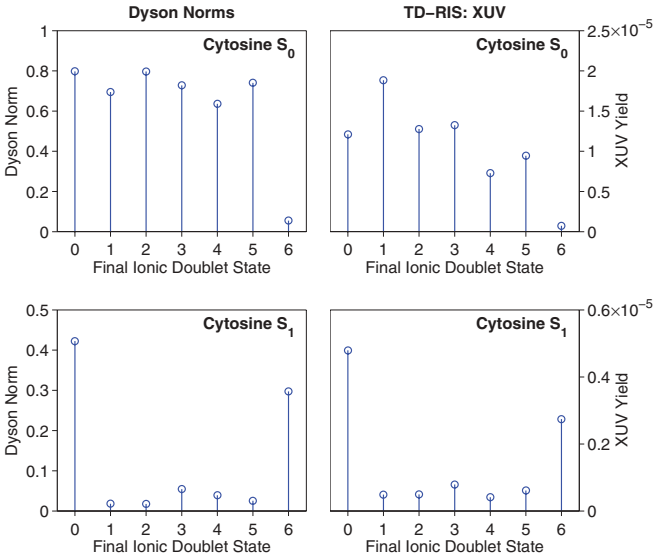

FIG. 1. (Color online) Comparison of the Dyson norms (left) with the TD-RIS XUV ionization yields (right) for ionization from the lowest two singlet states of cytosine (top, S_0; bottom, S_1).

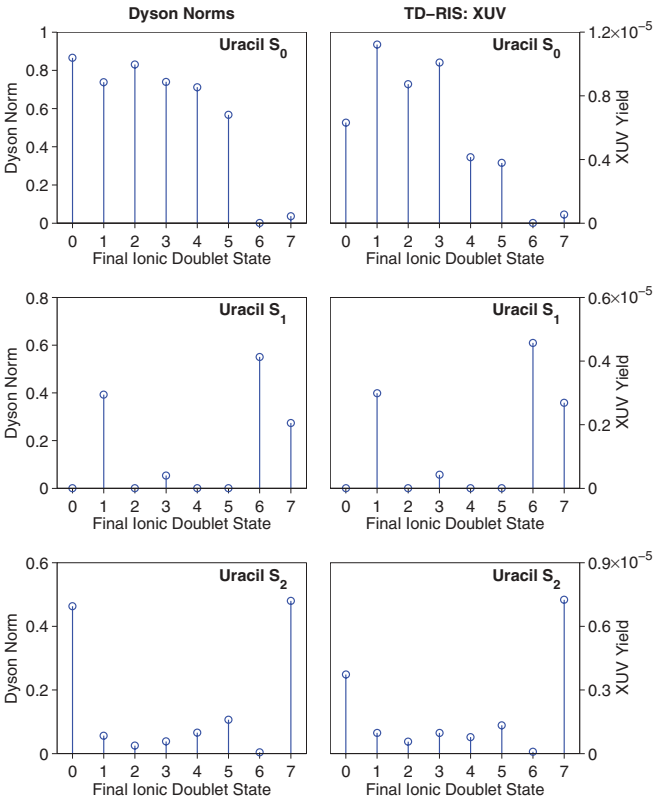

FIG. 2. (Color online) Comparison of the Dyson norms (left) with the TD-RIS XUV ionization yields (right) for ionization from the lowest three singlet states of uracil (top, S_0; middle, S_1; bottom, S_2).

III. COMPUTATIONAL RESULTS

A. One-photon XUV ionization

The connection between the Dyson norms and the one-photon XUV ionization yields is computationally demonstrated in Figs. 1 and 2, which show the Dyson norms (left columns) and TD-RIS ionization yields (right columns) for the lowest few neutral states of cytosine and uracil. The numerical XUV ionization yields were calculated using the TD-RIS method. The XUV pulse had the form

$$F(t) = F_0 f(t) \sin[\omega_X (t - \tau_{on})] \tag{22}$$

with a $\sin^2$ envelope

$$f(t) = \begin{cases} 0, & t < 0, \\ \sin^2\left(\frac{\pi t}{2\tau_{on}}\right), & 0 \leqslant t \leqslant 2\tau_{on}, \\ 0, & t > (2\tau_{on}). \end{cases} \tag{23}$$

The frequency and pulse width were $\omega_X = 4$ atomic units (a.u.) (108.8 eV) and $\tau_{on} = 20$ a.u. (0.48 fs), respectively. The peak electric field strength was $F_0 = 0.0378$ a.u. ($I_0 = 5 \times 10^{13}$ W/cm^2) for cytosine, and $F_0 = 0.0293$ a.u. ($I_0 = 3 \times 10^{13}$ W/cm^2) for uracil. Although these intensities are quite high, the ionization response is still within the perturbative one-photon regime at XUV frequencies.

Comparing the Dyson norms with the corresponding numerical ionization yields for Figs. 1 and 2 shows that the Dyson norms G^{D}_{lm} are indeed good predictors of the relative probabilities of one-photon XUV ionization. Although the G^{D}_{lm} are not strictly quantitative predictors of the relative ionization yields to the various cation states, the patterns of ionic-channel-resolved ionization probabilities seen in the right-hand columns is clearly reflected in the Dyson norms in the left-hand columns. Differences between the G^{D}_{lm} and the numerically calculated ionization probabilities are due to the presence of $\int d\vec{k}\, |\langle \phi^{\vec{k}}_l | \tilde{\phi}^{\mathrm{D}}_{lm} \rangle|^2$ and $\int d\vec{k}\, |\mathcal{F}(\omega_k)|^2 |\langle \phi^{\vec{k}}_l | \vec{\epsilon}_F \cdot \vec{r}_n | \tilde{\phi}^{\mathrm{D}}_{lm} \rangle|^2$ in the expressions for W^{sud}_{lm} and W^{1st}_{lm}, as well as the $|\phi^C_{lm}\rangle$ term used in the numerical simulations. However, these differences are relatively small and the general behavior of the ionic-channel-resolved yields are well characterized by the G^{D}_{lm} alone.

B. Strong-field ionization

In order to test Eq. (21), we calculated the strong-field ionization probability for the lowest few states of cytosine and uracil, integrating the time-dependent equations of motion over one half cycle of an 800-nm driving laser field. The peak electric field strength was again $F_0 = 0.0378$ a.u. ($I_0 = 5 \times 10^{13}$ W/cm^2) for cytosine, and $F_0 = 0.0293$ a.u. ($I_0 = 3 \times 10^{13}$ W/cm^2) for uracil. Unlike the XUV case, at 800 nm such intensities induce a strong nonlinear ionization response, and low-order perturbation theory is no longer applicable. Possible concerns regarding the use of a half-cycle pulse for low-frequency ionization are addressed in the Appendixes. The results of both the Dyson-Keldysh estimate and the numerical yields are shown in Figs. 3 and 4. In contrast to the comparison between the Dyson norms and the XUV ionization yields, here we see that the Dyson-Keldysh estimate, which takes into account the dominant exponential dependence of SFI and the Dyson norms, is no longer a good predictor of the relative probabilities of SFI to different cation states. The numerical simulations show much more population in excited cation states than would be expected from Eq. (21), the latter showing a very strong suppression of the excited cation

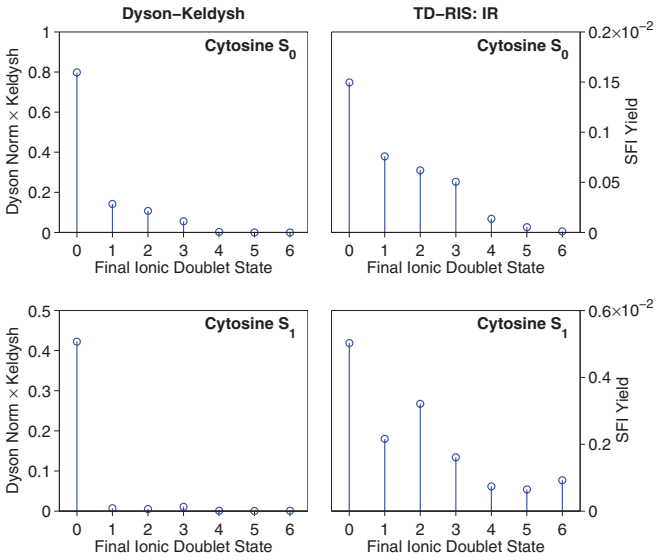

FIG. 3. (Color online) Comparison of the Dyson-Keldysh estimate (left) with the half-cycle strong-field ionization yields (right) for ionization from the lowest two singlet states of cytosine (top, S_0; bottom, S_1).

populations, particularly for ionization from excited states. The failure of the Dyson-Keldysh estimate as compared to the numerical results has two main sources: omission of the C_{lm} preexponential factor, and Coulomb-mediated interchannel coupling.

1. *Preexponential factor C_{lm}*

Unlike the case for one-photon XUV ionization, where the matrix elements $|\langle\phi_l^{\vec{k}}|\tilde{\phi}_{lm}^{\mathrm{D}}\rangle|^2$ and $|\langle\phi_l^{\vec{k}}|\vec{\epsilon}\cdot\vec{r}_n|\tilde{\phi}_{lm}^{\mathrm{D}}\rangle|^2$ could be neglected without detrimental effects, the factor C_{lm} is no longer weakly dependent on the final ionic state being populated. This difference between XUV and low-frequency ionization can be qualitatively understood as follows. In XUV ionization, the liberated electron makes a transition from the neutral directly to a high-lying continuum state. In the absence of strong continuum resonances, the high-lying continuum states depend weakly on the ionic core. Furthermore, the bound-continuum matrix elements $|\langle\phi_l^{\vec{k}}|\tilde{\phi}_{lm}^{\mathrm{D}}\rangle|^2$ and $|\langle\phi_l^{\vec{k}}|\vec{\epsilon}\cdot\vec{r}_n|\tilde{\phi}_{lm}^{\mathrm{D}}(x_n)\rangle|^2$ from XUV ionization in a sense "pick out" the large-momentum Fourier components from the Dyson orbitals. For large momentum, the Fourier spectrum of the different Dyson orbitals is smooth and shows little structure. In SFI, the continuum electron first slowly leaks out of the neutral into a low-lying continuum state and is then accelerated away from the core by the laser field once in the continuum. In this case, the process qualitatively involves a transition from the initial Dyson orbital into a low-lying field-distorted continuum state. This is the part of the process captured by the factor C_{lm}. Low-lying continuum states depend strongly on the structure of the ionic core, and thus on the particular final ion state accessed following ionization, leading to a large dependence of C_{lm} on the final ion state. This strong dependence, entering SFI qualitatively through the initial population of low-lying continuum states, is the main reason for the poor predictive power of Eq. (21).

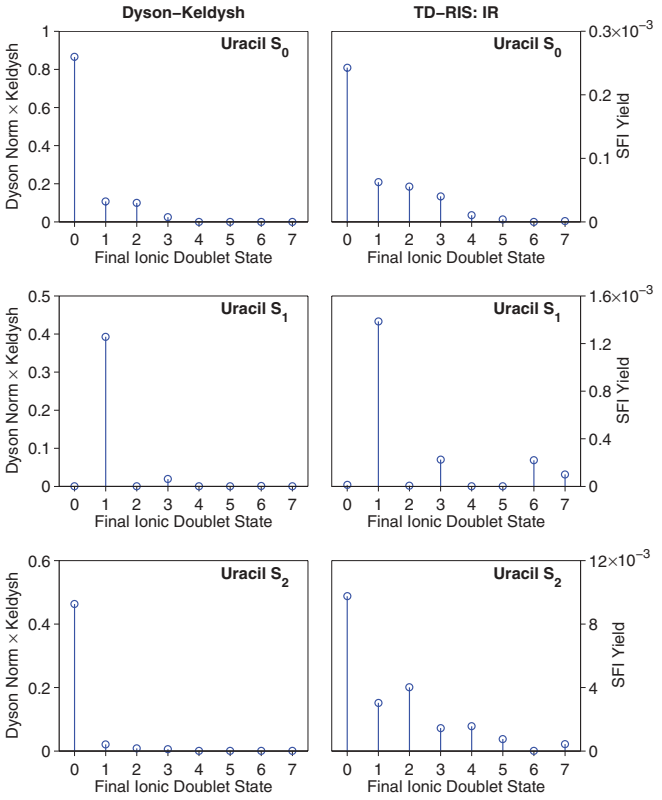

FIG. 4. (Color online) Comparison of the Dyson-Keldysh estimate (left) with the half-cycle strong-field ionization yields (right) for ionization from the lowest three singlet states of uracil (top, S_0; middle, S_1; bottom, S_2).

2. *Coulomb-mediated interchannel coupling*

The SFA model introduced above is a single-active-electron (SAE) model. Although this is a standard assumption in strong-field literature, it is of course not strictly valid. In fact, it is only very recently that theoretical efforts within the strong-field community have been focused on exploring non-SAE effects within the context of SFA models [18–20]. The computational model of Ref. [11], which we use for the numerical ionization yields, allows us to go beyond the SAE approximation. Of interest to the present discussion is the effect of the Coulomb force exerted by the continuum electron on the remaining bound ionic electrons: as the liberated electron is released and accelerated away from the parent molecule it can cause transitions in the ionic core through Coulomb interaction with the bound ionic electrons. Qualitatively, these are the same couplings responsible for autoionizing states. The couplings can be turned on or off at will in the simulations. Thus far, all simulations in Figs. 1–4 have left the couplings turned on. Figure 5 shows the effect of turning off the couplings in the XUV (left) and strong-field ionization (right), using the S_1 state of cytosine as an example. The interchannel coupling has very little effect in the XUV ionization. In this case, the liberated electron is ejected directly into a high-lying continuum state and quickly moves away from the parent, leaving little time for the Coulomb interaction to accumulate an appreciable effect [21]. In SFI, where the electron more slowly leaks out of the parent to be subsequently accelerated in the field, there is now comparatively more time for the Coulomb

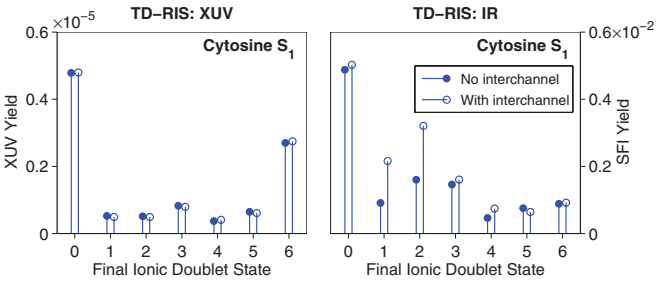

FIG. 5. (Color online) Comparison of the ionization calculations with (open circles) and without (solid circles) the Coulomb-mediated interchannel couplings for ionization from the S_1 of cytosine.

interactions to influence the ionization dynamics [19], and a sizable change in the ionization yields with and without the interchannel coupling is now seen for SFI, with the yield of states D_1 and D_2 increasing by almost a factor of 2.

3. *MO-ADK*

As a final consideration, we explore the results of the MO-ADK approach [12,13]. The MO-ADK method is used for calculating strong-field ionization rates of molecules based on quasistatic and semiclassical tunneling formulas. It has become a popular technique in studies of small molecules, largely due to the ease of computation of the final formulas. Building on previous results of Keldysh [15] and ADK [17] approaches, the MO-ADK method first decomposes the ionizing orbitals (in our case the Dyson orbital) into a spherical harmonic expansion at a large radius. It then applies the known tunneling formulas to each of the spherical components, within the approximation that the tunneling occurs through a long-range Coulomb barrier. Thus, the detailed structure of the nuclear binding potential is neglected for the ionization step. The MO-ADK method is intrinsically a single-active-electron method—ionization for each ionic channel is computed independently. Multielectron effects, such as the Coulomb-mediated interchannel couplings, are not included in the existing formulations. Figure 6 compares the MO-ADK ionization rates with the Dyson-Keldysh estimates for the case of uracil. We applied the spherical expansion at a radius of 9 a.u. about the center of mass of the molecules. Note that while the MO-ADK method calculates ionization rates, for short pulses and in the absence of complete neutral depletion the rates are proportional to the ionization yields. It is seen that the MO-ADK method mirrors the predictions of the Dyson-Keldysh estimates. Due to the fact that the MO-ADK method is not expected to be as rigorous a method as the TD-RIS method, we do not investigate further the detailed behavior of the MO-ADK results.

IV. DISCUSSION AND SUMMARY

In this study, we investigated one-photon XUV and strong-field IR ionization of cytosine and uracil, with emphasis on which final valence cation states are populated following the ionization. One-photon XUV ionization is well understood [8], and it is included in the present study as a background upon which we can discuss the strong-field ionization. Dyson norms are confirmed to act as good predictors of the population distribution across the valence cation states for XUV ionization.

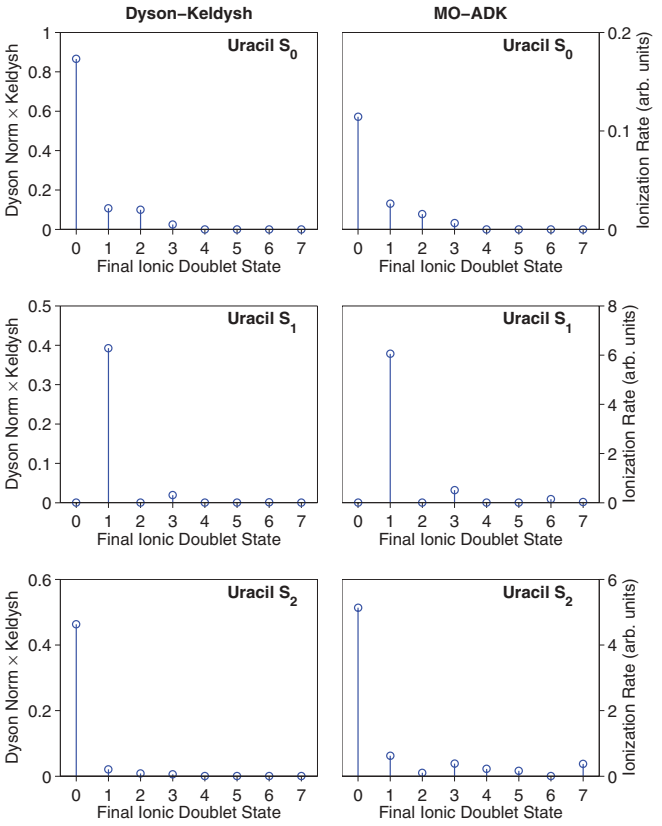

FIG. 6. (Color online) Ionic-state-resolved ionization rates for cytosine and uracil computed using the MO-ADK [12,13] method.

The analogous predictor for strong-field ionization, namely the Dyson-Keldysh estimate, is shown to be inadequate; the Dyson-Keldysh estimate consistently underestimates the ionization yield to excited cation states when compared against the more elaborate TD-RIS results. In addition, we have also evaluated the MO-ADK ionization theory for comparison. The MO-ADK method largely mirrors the results of the Dyson-Keldysh estimate.

Two sources of the breakdown of the Dyson-Keldysh estimate are captured and highlighted by the TD-RIS calculations. The first is the fact that the strong-field IR ionization couples initially to near-threshold continuum states where much continuum structure exists. Therefore, approximations that ignore low-lying continuum structure perform poorly. The second cause is the Coulomb-mediated interchannel coupling. It accounts for the Coulomb interaction between the excited (continuum) electron and the ionic core, which is again neglected in simple estimates such as the Dyson-Keldysh and the MO-ADK method. Not considered in the present study are the effects of laser-driven coupling of the neutral and/or the ionic bound states, which can lead to further deviations from the Dyson-Keldysh picture. Bound-state dynamics are briefly considered in the Appendixes, and those results suggest that while laser-driven coupling between the neutral bound states is not important in cytosine and uracil at the intensities used in the calculations, laser-driven coupling between ionic states can play a role in cytosine. Certainly any laser-driven resonances between the bound states will alter the yields, and furthermore, off-resonant nonadiabatic excitations can become important

in polyatomic molecules [5,22] at intensities typical of many strong-field experiments.

ACKNOWLEDGMENTS

We gratefully acknowledge the support from the US Department of Energy under Grants No. DE-FG02-08ER15983 and No. DE-PS02-08ER08-01.

APPENDIX A: HAMILTONIANS AND STATES

Within the nonrelativistic regime, the neutral H^N and ionic H^I Hamiltonians are

$$H^N = -\sum_{j=1}^{n}\frac{\nabla^2}{2} + \sum_{j=1}^{n} V_{\rm nuc}(\vec{r}_j) + \sum_{j=1}^{n}\sum_{k=j+1}^{n}\frac{1}{|\vec{r}_j - \vec{r}_k|} \quad \text{(A1)}$$

and

$$H^I = -\sum_{j=1}^{n-1}\frac{\nabla^2}{2} + \sum_{j=1}^{n-1} V_{\rm nuc}(\vec{r}_j) + \sum_{j=1}^{n-1}\sum_{k=j+1}^{n-1}\frac{1}{|\vec{r}_j - \vec{r}_k|}, \quad \text{(A2)}$$

where $V_{\rm nuc}(\vec{r})$ is the electrostatic potential of the nuclei. Hartree atomic units ($\hbar = m_e = e = 1$) are used throughout. These Hamiltonians give a set of neutral $|N_j\rangle$ and ionic $|I_j\rangle$ states

$$H^N|N_j\rangle = E_j^N|N_j\rangle, \quad \text{(A3a)}$$

$$H^I|I_j\rangle = E_j^I|I_j\rangle. \quad \text{(A3b)}$$

The laser-matter interaction is included in the (length gauge) dipole approximation,

$$H^F(t) = H^N + V(t), \quad \text{(A4)}$$

where

$$V(t) = \sum_{j=1}^{n} F(t)\,\vec{\epsilon}_F\cdot\vec{r}_j, \quad \text{(A5)}$$

$F(t)$ is the time-dependent electric field of the laser, and $\vec{\epsilon}_F$ is the polarization direction.

APPENDIX B: TIME-DEPENDENT RESOLUTION IN IONIC STATES (TD-RIS) APPROACH

In the numerical approach of Ref. [11], referred to herein as the TD-RIS approach, the wave-function ansatz uses a time-dependent unsymmetrized version of $|\mathcal{M}_j\rangle$ to represent the continuum-ion space,

$$|\mathcal{M}'(t)\rangle = \sum_m |X_m(t)\rangle, \quad \text{(B1)}$$

where

$$|X_m(t)\rangle = |I_m\rangle|\chi_m(t)\rangle, \quad \text{(B2)}$$

and the $|\chi_m(t)\rangle$ are time-dependent continuum wave packets (i.e., not continuum energy eigenstates). Neglecting $\widehat{\mathcal{A}}$ is presently necessary in the numerical simulations in order to yield equations of motion that can be numerically solved in a reasonable time. Although antisymmetrization is not fully included in the numerical codes, we can still use the simulations to investigate a number of effects not uniquely related to antisymmetrization.

The TD-RIS method of Ref. [11] proceeds to derive the equations of motion for the $|\chi_m(t)\rangle$ states coupled to a neutral initial state $|N_j\rangle$. To this end, a set of "Dyson-ion" states $|S_{lm}\rangle$ are introduced:

$$|S_{lm}\rangle = \left|\tilde{\phi}^{\rm D}_{lm}\right\rangle|I_{lm}\rangle. \quad \text{(B3)}$$

Next we introduce the component of the neutral ground state that is orthogonal to the set of $|S_{lm}\rangle$ states,

$$\begin{aligned}|\tilde{N}_m\rangle &= \mathcal{N}_{\tilde{N}}\left(\widehat{I} - \sum_l |S_{lm}\rangle\langle S_{lm}|\right)|N_m\rangle \\ &= \mathcal{N}_m\left[|N_m\rangle - \sum_l \eta_{lm}|S_{lm}\rangle\right], \end{aligned} \quad \text{(B4)}$$

where $\mathcal{N}_m$ is the normalization factor of the state $|\tilde{N}_m\rangle$. The full ansatz underlying the method of Ref. [11] can now be written as

$$|\Psi(t)\rangle = b(t)|\tilde{N}_m\rangle + \sum_l [a_l(t)|S_{lm}\rangle + |X_l(t)\rangle], \quad \text{(B5)}$$

where $a_l(t)$ and $b(t)$ are presently unknown time-dependent amplitudes of the $|S_{lm}\rangle$ and $|\tilde{N}_m\rangle$ states. By inserting this ansatz into the Schrödinger equation (where $\partial_t = \partial/\partial t$)

$$i\,\partial_t|\Psi(t)\rangle = H^F(t)|\Psi(t)\rangle, \quad \text{(B6)}$$

a coupled set of Schrödinger equations for $a_l(t)$, $b(t)$, and $|\chi_{lm}(t)\rangle$ is obtained:

$$\begin{aligned} i\,\partial_t b(t) &= \langle\tilde{N}|H^F(t)|\tilde{N}\rangle b(t) + \sum_k \langle\tilde{N}|H^F(t)|S_k\rangle a_k(t) \\ &\quad + \sum_k \langle\tilde{N}|H^F(t)|X_k(t)\rangle, \\ i\,\partial_t a_m(t) &= \langle S_m|H^F(t)|\tilde{N}\rangle b(t) + \sum_k \langle S_m|H^F(t)|S_k\rangle a_k(t) \\ &\quad + \sum_k \langle S_m|H^F(t)|X_k(t)\rangle, \\ i\,\partial_t|\chi_m(t)\rangle &= \widehat{\mathcal{R}}^S_m\langle I_m|H^F(t)|\tilde{N}\rangle b(t) \\ &\quad + \sum_k \widehat{\mathcal{R}}^S_m\langle I_m|H^F(t)|S_k\rangle a_k(t) \\ &\quad + \sum_k \widehat{\mathcal{R}}^S_m\langle I_m|H^F(t)|X_k(t)\rangle, \end{aligned} \quad \text{(B7)}$$

where $\widehat{\mathcal{R}}^S_m = (1 - |\tilde{\phi}^S_m\rangle\langle\tilde{\phi}^S_m|)$. All the required matrix elements of $H^F(t)$ are given in the appendix of Ref. [11]. This is the set of coupled equations that our computational method implements.

APPENDIX C: DETAILS OF IMPLEMENTATION

In the numerical TD-RIS results, Eqs. (B7) are numerically integrated in time using the leapfrog algorithm, which is low -order but easily parallelizable. The continuum functions $|\chi_m(t)\rangle$ are represented on Cartesian grids with a grid-point spacing of 0.2 a.u. The grids extended to ± 15 a.u. in all three spatial directions. The time step was $dt = 0.0026666$ a.u.; such a small time step is required for the leapfrog algorithm to ensure numerical stability. Absorbing boundaries [23] of width 4.5 a.u. are used at the grid edges to absorb the outgoing free-electron flux, and the total ionization yields were calculated by monitoring the absorbed flux. Angular averaging over the

relative angle between the molecular axis and the polarization direction of the laser is carried out using Lebedev angular grids of the ninth order [24], which can accurately represent angular structures up to about the fifth-order spherical harmonics.

The ionization calculations are carried out at the neutral ground-state (S_0) geometry, calculated in previous studies [6]. For the present study, the low-lying neutral and cation states (S_0–S_1 and D_0–D_6 for cytosine, S_0–S_2 and D_0–D_7 for uracil) were calculated at the multiconfiguration self-consistent field calculation (MCSCF) level using GAMESS-US [25]. The neutral (cation) active space included 14 (13) electrons in 10 orbitals, and the aug-cc-pVDZ basis set (as implemented in GAMESS-US) was used. The MCSCF calculations used state averaging over the neutral and cation states independently.

APPENDIX D: ELECTRONIC CONFIGURATIONS AND MOLECULAR ORBITALS

Figure 7 shows the dominant electronic configurations and participating orbitals for the neutral and ionic states of uracil and cytosine. These configurations illustrate why there is a large Dyson norm between the bright excited states of cytosine and uracil (S_1 and S_2, respectively) and their ground ionic states (D_0), while the Dyson norms for these neutral states and the first few ionic states (D_1–D_3) are very low. The configuration for the ground ionic states differs from the excited neutral state configurations only by the removal of one electron, whereas the exited ionic states involve removal of an electron in conjunction with further rearrangement.

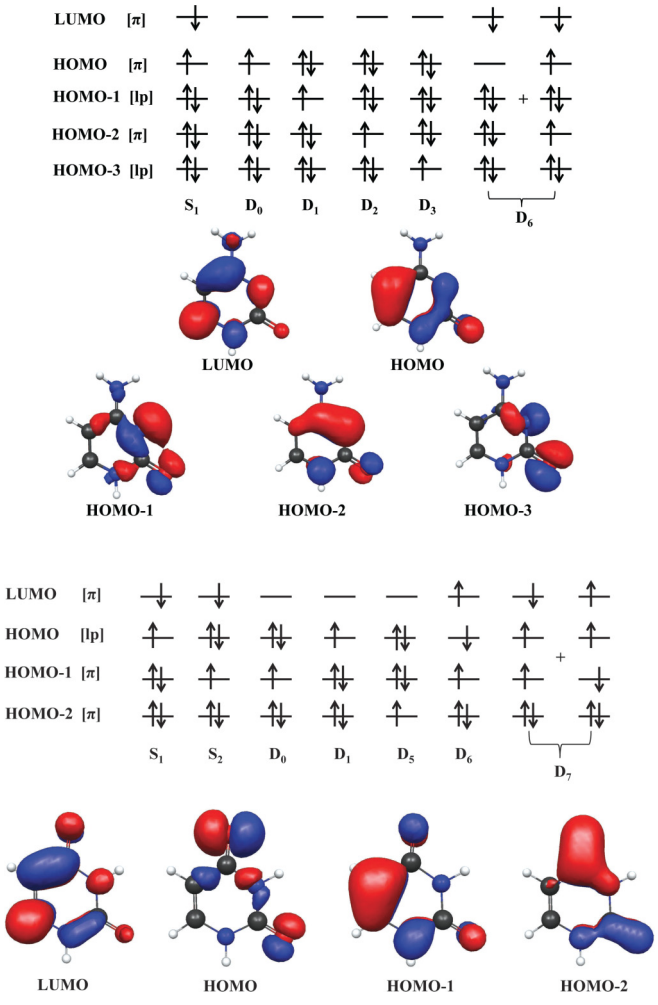

FIG. 7. (Color online) Dominant electronic configurations for relevant states of the neutral and the ion for cytosine (top) and uracil (bottom). The participating orbitals are shown as well. Whenever there is an approximately equal contribution from more than one configuration, both of them are shown in the figure. The orbitals shown are taken from the MCSCF calculation on the neutral molecule and are only qualitative for the ions.

APPENDIX E: BOUND-STATE DYNAMICS

In order to estimate the importance of laser-driven coupling between the neutral or cation bound states, we performed explicit calculations of the laser-coupled bound-state systems. In these calculations, all population was initialized in the corresponding ground state (S_0 for the neutrals, D_0 for the cations). We then solved the time-dependent Schrödinger matrix equation in the basis of bound states, in the absence of ionization:

$$i\frac{\partial}{\partial t}\begin{bmatrix} c_0^I(t) \\ c_1^I(t) \\ c_2^I(t) \\ \vdots \end{bmatrix} = \begin{bmatrix} E_0+\mu_{00}^I(t) & \mu_{01}^I(t) & \\ \mu_{10}^I(t) & E_1+\mu_{11}^I(t) & \cdots \\ & \vdots & \ddots \end{bmatrix} \times \begin{bmatrix} c_0^I(t) \\ c_1^I(t) \\ c_2^I(t) \\ \vdots \end{bmatrix}, \tag{E1}$$

where E_n are the field-free energies of the bound states, the $c_m^I(t)$ are the amplitudes of the bound states, and the $\mu_{nm}^I(t) = \vec{F}(t)\cdot\langle\Psi_n|\sum_i \vec{r}_i|\Psi_m\rangle$ account for the laser interaction with

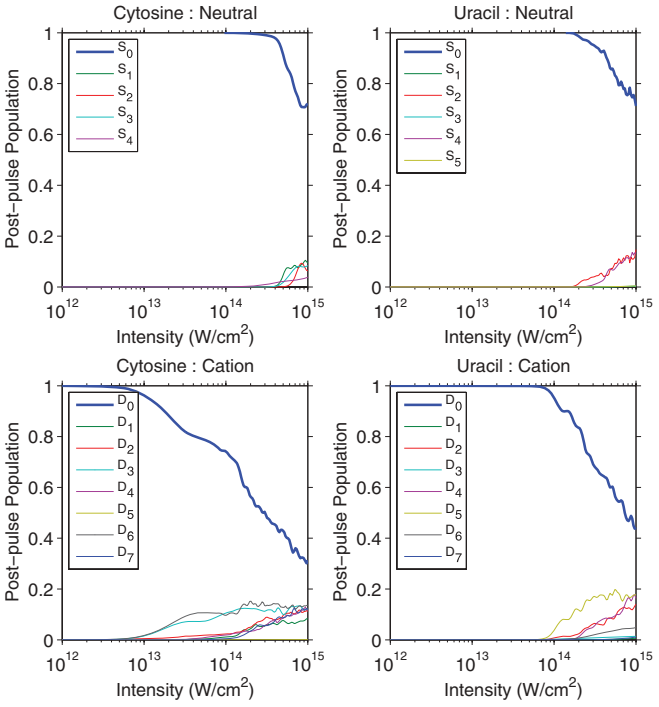

FIG. 8. (Color online) Nonadiabatic bound-state dynamics.

the permanent and transition dipoles of the field-free states. We solve the matrix equation for the system of bound states interacting with a 30-fs $\sin^2$ pulse at 800 nm, where we take 30 fs to be a typical ultrafast pulse duration. The final populations of the bound states are shown in Fig. 8. For most cases, there is no significant postpulse population left in any excited bound states for intensities below 1×10^{14} W/cm^2, indicating that nonadiabatic laser-driven coupling between the bound states is not significant at these intensities, thus justifying the exclusion of the laser-driven coupling in the TD-RIS calculations. The case of the cytosine cation shows a lower intensity threshold than the other cases for the laser-driven coupling. Investigation of the effects of laser-driven coupling on the TD-RIS calculations is left for future studies.

APPENDIX F: HALF CYCLE VERSUS FULL PULSE

Strong-field ionization for the low-frequency regime is calculated using a half-cycle pulse. This is done due to the computational workload involved with the TD-RIS method. It is simply not feasible with present implementations to calculate the range of results covered in this paper using a full pulse at 800 nm wavelength. Since the XUV pulse is much shorter in total duration, full-pulse calculations are feasible for the attosecond XUV pulses.

At first glance, this may cause some concern, since a half-cycle pulse is not consistent with the free-space Maxwell wave equations. Here we justify the use of the half-cycle pulse. First, it should be noted that, for low-frequency fields, the tunneling process occurs largely by quasistatic tunneling ionization in the combined potential of the cation plus the laser field; the strong laser tilts the binding potential of the cation and the liberated electron escapes through the suppressed barrier. Indeed, traditional analytical treatments of low-frequency ionization, like the ADK theory [17], calculate the static-field ionization rate and then average the static-field result over the single cycle. In addition to analogy with the traditional analytical treatments, we included a single test case where we compare the half-cycle pulse against a full pulse [4.8 fs full width at half maximum (FWHM)] for the IR ionization, shown in Fig. 9. As can be seen, there are small variations between the two results, but qualitatively the half-cycle pulse captures the general features of the full-pulse simulation. Importantly, the failure of the Dyson-Keldysh estimate is not caused by half-cycle artifacts.

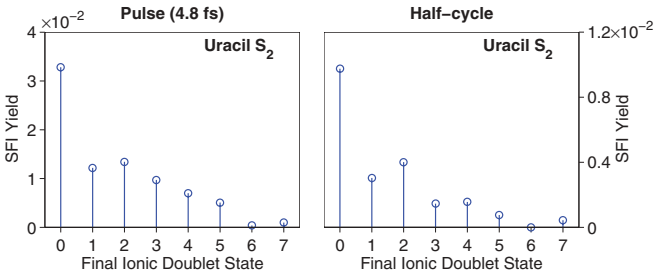

FIG. 9. (Color online) Ionization of the S_2 state of uracil for a full pulse (4.8-fs FWHM envelope) and a half-cycle pulse.

[1] F. Krausz and M. Ivanov, Rev. Mod. Phys. **81**, 163 (2009).

[2] P. B. Corkum, Phys. Rev. Lett. **71**, 1994 (1993).

[3] S. X. Hu and L. A. Collins, Phys. Rev. Lett. **96**, 073004 (2006).

[4] S. Baker, J. S. Robinson, C. A. Haworth, H. Teng, R. A. Smith, C. C. Chirilă, M. Lein, J. W. G. Tisch, and J. P. Marangos, Science **312**, 424 (2006); O. Smirnova, Y. Mairesse, S. Patchkovskii, N. Dudovich, D. Villeneuve, P. Corkum, and M. Yu. Ivanov, Nature (London) **460**, 972 (2009); H. J. Wörner, J. B. Bertrand, B. Fabre, J. Higuet, H. Ruf, A. Dubrouil, S. Patchkovskii, M. Spanner, Y. Mairesse, V. Blanchet, E. Mével, E. Constant, P. B. Corkum, and D. M. Villeneuve, Science **334**, 208 (2011).

[5] M. Spanner, J. Mikosch, A. Gijsbertsen, A. E. Boguslavskiy, and A. Stolow, New J. Phys. **13**, 093010 (2011); A. E. Boguslavskiy, J. Mikosch, A. Gijsbertsen, M. Spanner, S. Patchkovskii, N. Gador, M. J. J. Vrakking, and A. Stolow, Science **335**, 1336 (2012).

[6] M. Kotur, T. C. Weinacht, C. Zhou, K. A. Kistler, and S. Matsika, J. Chem. Phys. **134**, 184309 (2011); M. Kotur, T. C. Weinacht, C. Zhou, and S. Matsika, Phys. Rev. X **1**, 021010 (2011).

[7] T. Koopmans, Physica **1**, 104 (1934).

[8] B. T. Pickup, Chem. Phys. **19**, 193 (1977).

[9] Y. Öhrn and G. Born, Adv. Quantum Chem. **133**, 1 (1981).

[10] For some examples from a variety of groups see M. Mishra and Y. Öhrn, J. Quantum Chem **14**, 335 (1980); I. Cacelli, V. Carravetta, and R. Moccia, J. Phys. B **16**, 1895 (1983); O. Dolgounitcheva, V. G. Zakrzewski, and J. V. Ortiz, J. Phys. Chem. A **107**, 822 (2003); C. Melania Oana and A. I. Krylov, J. Chem. Phys. **127**, 234106 (2007); S. Han and D. R. Yarkony, *ibid.* **134**, 134110 (2011).

[11] M. Spanner and S. Patchkovskii, Phys. Rev. A **80**, 063411 (2009).

[12] X. M. Tong, Z. X. Zhao, and C. D. Lin, Phys. Rev. A **66**, 033402 (2002).

[13] S.-F. Zhao, J. Xu, C. Jin, A.-T. Le, and C. D. Lin, J. Phys. B **44**, 035601 (2011).

[14] W. A. Friedman, Ann. Phys. **45**, 265 (1967).

[15] L. V. Keldysh, Zh. Eksp. Teor. Fiz. **47**, 1945 (1964) [Sov. Phys. JETP **20**, 1307 (1965)].

[16] A. M. Perelomov, V. S. Popov, and M. V. Terent'ev, Zh. Eksp. Teor. Fiz. **50**, 1393 (1966) [Sov. Phys. JETP **23**, 924 (1966)]; Zh. Eksp. Teor. Fiz. **51**, 309 (1966) [Sov. Phys. JETP **24**, 207 (1967)].

[17] M. V. Ammosov, N. B. Delone, and V. P. Krainov, Zh. Eksp. Teor. Fiz. **91**, 2008 (1986) [Sov. Phys. JETP **64**, 1191 (1986)].

[18] Y. Mairesse, J. Higuet, N. Dudovich, D. Shafir, B. Fabre, E. Mével, E. Constant, S. Patchkovskii, Z. Walters, M. Yu. Ivanov, and O. Smirnova, Phys. Rev. Lett. **104**, 213601 (2010).

[19] Z. B. Walters and O. Smirnova, J. Phys. B **43**, 161002 (2010).

[20] S. Patchkovskii, O. Smirnova, and M. Spanner, J. Phys. B **45**, 131002 (2012).

[21] The presence of strong Coulomb-mediated interchannel coupling in XUV photoionization is possible; an example is the so-called giant resonances found in high-frequency ionization of atoms.
[22] M. Lezius, V. Blanchet, D. M. Rayner, D. M. Villeneuve, A. Stolow, and M. Yu. Ivanov, Phys. Rev. Lett. **86**, 51 (2001).
[23] D. E. Manolopoulos, J. Chem. Phys. **117**, 9552 (2002).
[24] V. I. Lebedev, USSR Comp. Math. Math. Phys. **15**, 44 (1975).
[25] M. W. Schmidt, K. K. Baldridge, J. A. Boatz, S. T. Elbert, M. S. Gordon, J. H. Jensen, S. Koseki, N. Matsunaga, K. A. Nguyen, S. Su, T. L. Windus, M. Dupuis, and J. A. Montgomery, J. Comput. Chem. **14**, 1347 (1993).